

Structural and superconducting parameters of highly compressed sulfur

Evgeny F. Talantsev^{1,2}, Evgeniya G. Valova-Zaharevskaya¹,

¹M. N. Miheev Institute of Metal Physics, Ural Branch, Russian Academy of Sciences, 18, S. Kovalevskoy St., Ekaterinburg 620108, Russia

²NANOTECH Centre, Ural Federal University, 19 Mira St., Ekaterinburg 620002, Russia

Abstract

Sulfur was the first nonmetal element which was transformed to a superconductor by applying megabar pressure. Recent pioneering experimental developments in measuring the superconducting energy gap $\Delta(T)$ in compressed sulfur using tunneling spectroscopy (Du et al., *Phys. Rev. Lett.* **133**, 036002 (2024)) initiated an interest in better understanding real atomic structure and superconducting properties of this element at high pressure. Here, we analyzed available experimental data on highly compressed sulfur, and, from the $\Delta(T)$ data reported by Du et al. (2024), we extracted the specific heat jump at the transition temperature of $\Delta C_{el}/\gamma T_c = 1.8$. We also developed a model to extract the Debye temperatures Θ_D for sulfur and H₃S in two-phases sample from the temperature-dependent resistance $R(T)$. for better understanding of material structure, here we proposed to use a size-strain map for highly compressed samples, and we revealed this size-strain map for laser-heated sulfur in a diamond anvil cell with a mixture of sulfur and H₃S. Finally, we found that superconducting sulfur exhibits a moderate level of nonadiabaticity $0.04 \leq \Theta_D/T_F \leq 0.15$ (where T_F is the Fermi temperature), which is similar to MgB₂, pnictides, cuprates, La₄H₂₃, ThH₉, H₃S, LaBeH₈, and LaH₁₀.

Keywords: high-pressure superconductivity; size-strain analysis; temperature dependent superconducting energy gap; specific heat jump at the transition temperature; Debye temperature.

Structural and superconducting parameters of highly compressed sulfur

I. Introduction

Yakovlev *et al.*¹ were the first to transform insulating element into a superconductor by applying high pressure. This non-metallic element was sulfur. Since then, highly pressurized sulfur and other non-metallic elements, which transform into superconductors by applying high pressure, were studied for nearly five decades²⁻¹⁷. A revival of interest in superconducting sulfur followed the landmark discovery of near-room-temperature superconductivity in highly compressed H₃S¹⁸, where elemental sulfur can be used as a starting material for the synthesis of the H₃S phase¹⁹⁻²⁴. The phase is in a focus of extended experimental and theoretical studies^{22,25-46}.

Very recent interest in highly compressed sulfur originates from several studies^{7,12-15,23}. Here, in attempt to improve our understanding of the extremely diverse phase diagram and physical properties of highly compressed sulfur, we have performed further analysis of experimental data reported in four recent studies:

- (1) Du *et al.*¹² reported a ground-breaking experimental development to measure the superconducting energy gap, $\Delta(T)$, in a superconductor (e.g., sulfur) at megabar pressure using tunnelling spectroscopy technique;
- (2) Wang *et al.*¹³ reported that at some pressure range, P , highly compressed sulfur has in-field temperature dependent resistance, $R(T, B, P)$, similar to those in underdoped ambient pressure cuprates;
- (3) Osmond *et al.*²³ reported experimental data on highly compressed two-phase sample H₃S+S from which the properties of elemental sulfur have been deduced in the current study;

(4) Shi *et al*¹⁴ further extended the phase diagram of sulfur by investigating the structure of sulfur after fast ramp compression.

II. Data sources and theoretical models

Analysis was performed for datasets which are freely available online^{12–14,23}. The experimental conditions under which the X-ray diffraction scans of highly compressed sulfur were obtained are given in the corresponding experimental parts of the original reports. The raw X-ray diffraction data were first analyzed using Dioptas⁴⁷ software. Descriptions of the developed model for temperature-dependent resistance and the well-known models used are given in the corresponding sections.

III. Results and Discussion

3.1. Sulfur in a tunnel junction at $P = 160$ GPa.

Du *et al.*¹² measured temperature dependent gap amplitude, $\Delta(T)$, in sulfur compressed at $P = 160$ GPa. It should be noted that Gross *et al.*^{48,49} proposed simple analytical equation for temperature dependent gap for the s -wave symmetry:

$$\Delta(T) = \Delta(0) \times \tanh \left[\frac{\pi k_B T_c}{\Delta(0)} \times \sqrt{\eta \times \frac{\Delta C_{el}}{\gamma T_c} \times \left(\frac{T_c}{T} - 1 \right)} \right], \quad (1)$$

where k_B is the Boltzmann constant, $\eta = \frac{2}{3}$ for superconductors exhibited s -wave symmetry, $\frac{\Delta C_{el}}{\gamma T_c}$ is one of several universal unit-less ratios of the Bardeen-Cooper-Schrieffer⁵⁰ theory, which is the relative jump in the electronic heat at T_c , and γ is the Sommerfeld parameter.

Based on this, we fitted the $\Delta(T)$ dataset¹² to Eq. 1 (where $\Delta(0)$, T_c , and $\frac{\Delta C_{el}}{\gamma T_c}$ are free fitting parameters) to deduce unknown fundamental ratio $\frac{\Delta C_{el}}{\gamma T_c}$ for highly compressed sulfur, in addition

to $\Delta(0)$ and T_c . The fit is shown in Fig. 1 and deduced ratios are $\frac{\Delta C_{el}}{\gamma T_c} = 1.8 \pm 0.1$ and $\frac{2\Delta(0)}{k_B T_c} =$

3.89 ± 0.06 . It is evident that the obtained value $\frac{2\Delta(0)}{k_B T_c}$ is within the uncertainty intervals for the

value $\frac{2\Delta(0)}{k_B T_c} = 3.8$ reported by Du *et al.*¹².

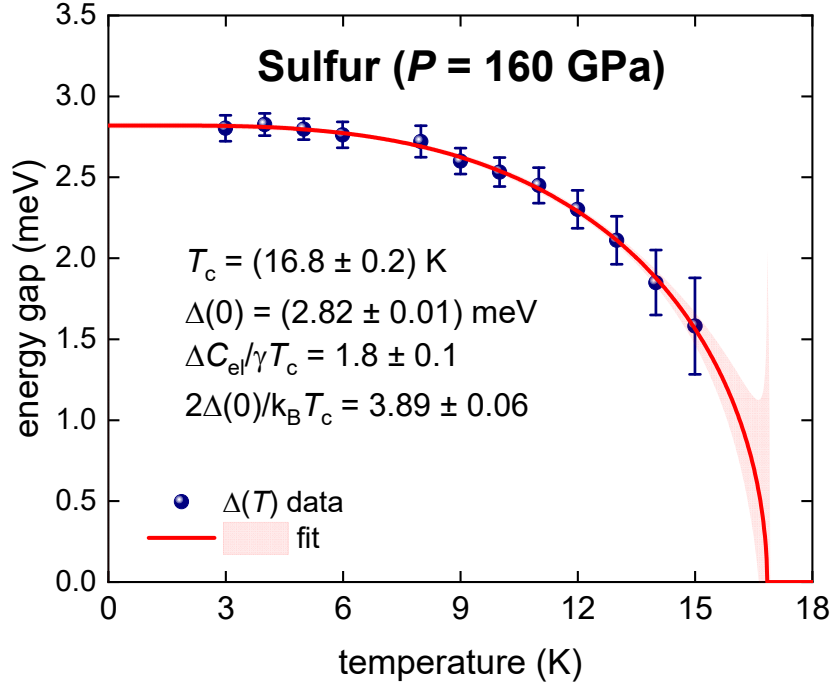


Figure 1. Superconducting gap values, $\Delta(T)$, in compressed sulfur ($P = 160$ GPa) measured by Du *et al.*¹² and data fit to Gross *et al.*^{48,49} model. Deduced values are shown. 95% confidence intervals are indicated by the pink shaded area. Fit quality R-Squared (COD) = 0.9948.

To demonstrate that deduced $\frac{\Delta C_{el}}{\gamma T_c}$ and $\frac{2\Delta(0)}{k_B T_c}$ for highly compressed sulfur (Fig. 1) are well aligned with general trend established for 34 classical ambient-pressure electron-phonon superconductors by Carbotte⁵¹, in Fig. 2 we showed the datapoint for compressed sulfur together with full dataset reported by Carbotte⁵¹.

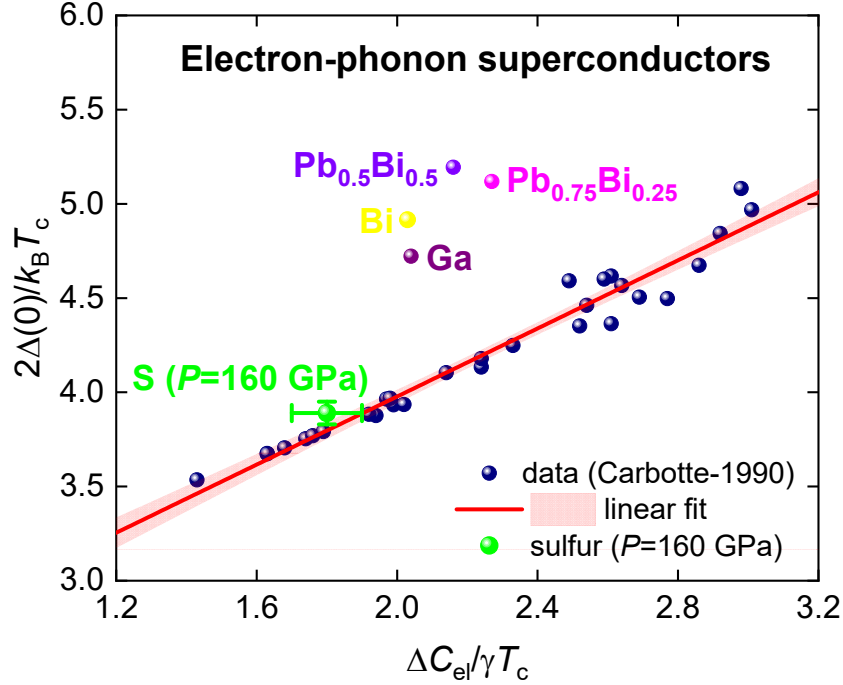


Figure 2. $\frac{2\Delta(0)}{k_B T_c}$ vs $\frac{\Delta C_{el}}{\gamma T_c}$ datapoint for highly compressed sulfur ($P=160$ GPa) derived herein and dataset for 34 ambient pressure classical electron-phonon superconductors reported by Carbotte⁵¹. Data for Ga, Bi, $Pb_{0.5}Bi_{0.5}$, $Pb_{0.75}Bi_{0.25}$ and S($P=160$ GPa) are not included in the linear fit. 95% confidence intervals are indicated by the pink shaded area.

3.2. Hysteretic $R(T, B, P)$ curves of sulfur at $P = 93$ -196 GPa

Wang *et al*¹³ made publicly available several raw $R(T \leq 280$ K, $B \leq 9$ T, 93 GPa $\leq P \leq 196$ GPa) datasets for sulfur which we examined in details herein. In their paper, Wang *et al*¹³ reported on the negative slope of the resistance in sulfur-phase-V at applied field 0 T $\leq B \leq 1$ T and temperature range of $T = 2 - 30$ K.

Closer examination of raw $R(T, B, P)$ datasets¹³, however, revealed a more complicated picture. For instance, in Fig. 3 we showed full $R(T, 0$ T $\leq B \leq 1.0$ T, $P = 163$ GPa) dataset, which was only partially shown by Wang *et al*¹³ in their Fig. 2,^{a13}.

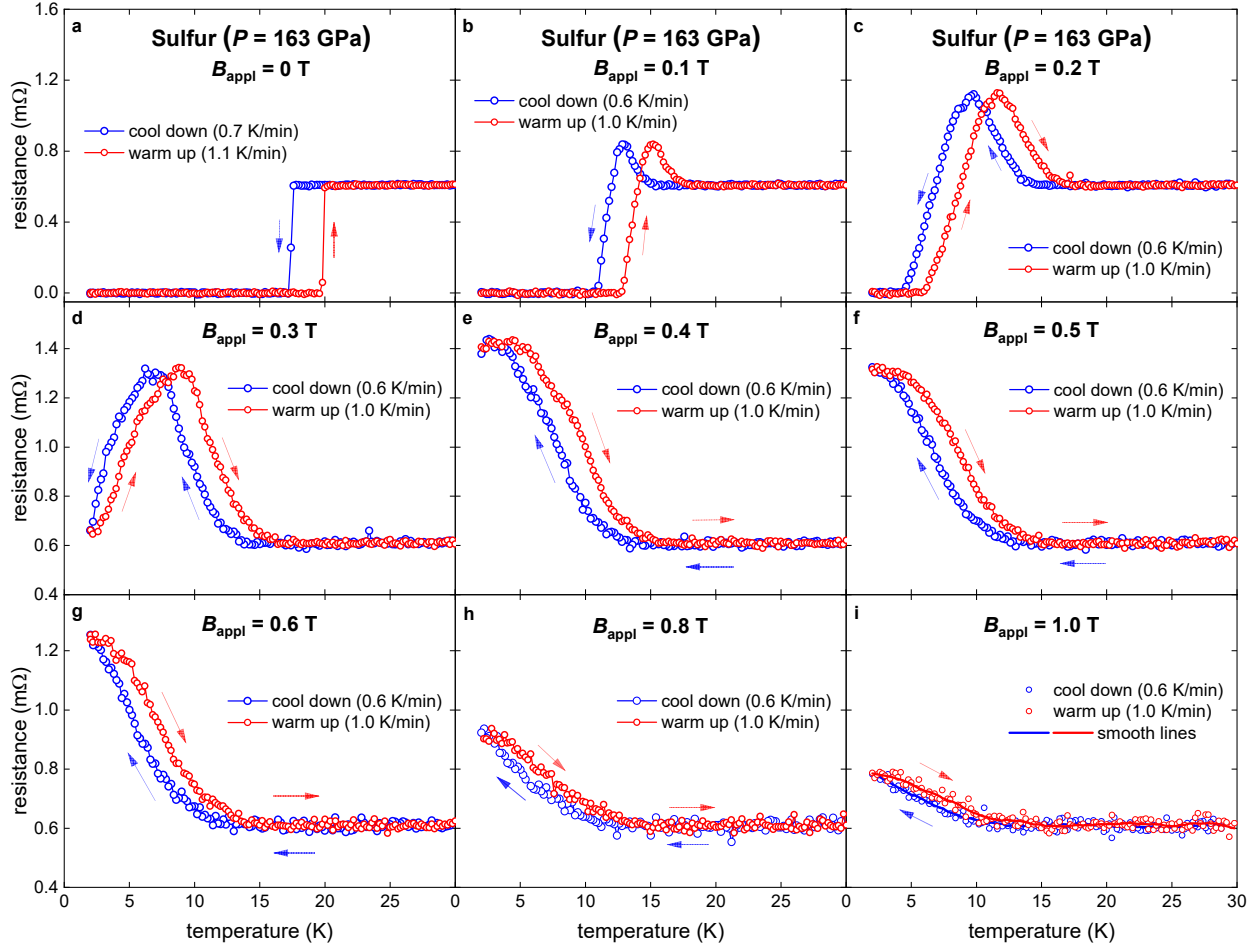


Figure 3. $R(T, B, P = 163 \text{ GPa})$ in compressed sulfur measured by Wang *et al*¹³ and partially reported in Fig. 2,a¹³. All experiments started at $T = 30 \text{ K}$ at the settled magnetic field B_{appl} , and then the sample was cooled down to $T = 2 \text{ K}$ and warmed up with indicated rates.

It is evident from Fig. 3, that the $R(T, B, P)$ curves demonstrate prominent hysteresis.

We can propose/discuss several explanations for the observed hysteresis (Fig. 3). First of all, we need to stress that elemental sulfur exhibits more than 30 allotropic phases at normal conditions⁵² and, thus, any observed hysteresis for some physical property can be associated with one of many possible phase transitions. The second, as it was mentioned by Ma *et al.*⁵³ the pressure in DAC has trend to increase in the thermal cycling. Based on this, the $R(T, B, P)$ measurements as a rule are performing on the warming semi-cycle⁵³. The third reason for the observed hysteresis in Fig. 3 is that the cooling-warming rates ($\sim 1 \text{ K/min}$) used by Wang *et al*¹³

were too fast that the sample and the DAC can reach thermal equilibrium with the PPMS chamber. This hypothesis can get further support by considering full raw $R(T, B = 0, P = 93 \text{ GPa})$ dataset¹³ (Fig. 4), which was partially showed by Wang *et al*¹³ in their Fig. 1¹³. One can see the large difference between the $R(T, B = 0, P = 93 \text{ GPa})$ measured at cooling rate of 0.7 K/min and warming rate of 2.0 K/min. However, we should pointed out again, that the issue with different pressure at the cooling and warming stages⁵³ in DAC can be the reason for the observed hysteresis in Fig. 4.

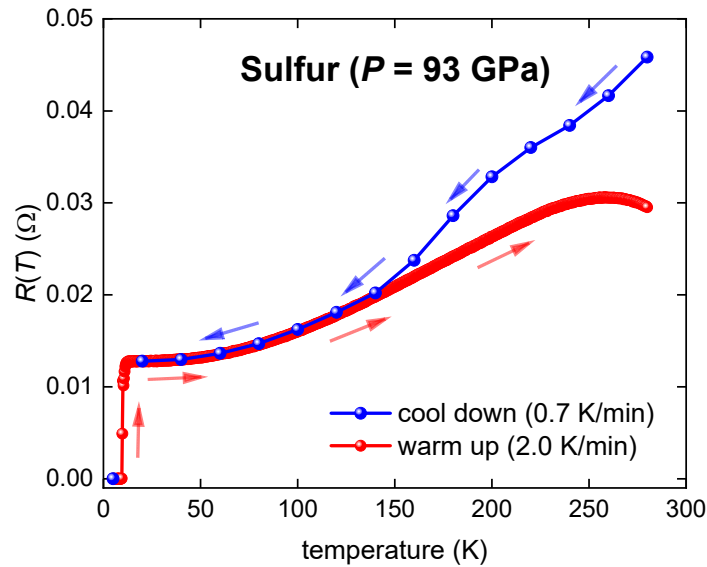


Figure 4. $R(T, B, P = 93 \text{ GPa})$ in compressed sulfur measured by Wang *et al*¹³ and partially reported in Fig. 1,^{a13}. The sample at $B_{\text{appl}} = 0$ was cooled down from $T = 280 \text{ K}$ to $T = 2 \text{ K}$ with rates of 0.7 K/min, and then warmed up to $T = 280 \text{ K}$ with the rate 2.0 K/min.

The fifth probable explanation is that, at this temperature-pressure range and used cooling-warming rates, the compressed sulfur exhibits two-phase state, where one phase can be one-dimensional charge-density wave (CDW) phase with transition at $T \sim 150 \text{ K}$ (this is just an estimate based on Fig. 4). CDW transition in compressed sulfur was proposed by Degtyareva *et al*.¹⁰. The CDW can affect the $R(T, B, P)$ in a hysteretic manner, similar to hysteretic $R(T)$ curves⁵⁴⁻⁵⁶ reported for the IrTe₂, where stripe-charge ordering and phase structural transitions

occur at $T < 300 \text{ K}$ play a dominant role in the emergence of the superconductivity⁵⁷ in IrTe₂. Based on this, we propose that the cooling-warming conditions in high-pressure studies need to be reported, and the rate for the cooling-warming cycle should be lower than 2.0 K/min.

To some extent, all $R(T, P)$ curves measured by Wang *et al*¹³ in highly compressed sulfur are hysteretic (which can be seen in raw data¹³). Considering a fact that the same team performed high-pressure resistance measurements in Ref.⁵⁸, more experimental data is required to results reported in Ref.⁵⁸, because the $R(T, P)$ curves in Ref.⁵⁸ have been reported at the cooling semi-cycle only, and there is no data for the warming part of all cycles.

Below we analyzed the $R(T, B = 0, P)$ datasets¹³ measured at the warming stage, because the $R(T, B = 0, P)$ datasets¹³ at the cooling stage do not have enough raw data for the analysis, and pressure stabilization in DAC at this semicycle⁵³.

3.3. Pressure dependence of the transition temperature, Debye temperature and the electron-phonon coupling constant

Bardeen-Cooper-Schrieffer (BCS) theory⁵⁰ predicts that pressure should suppress the T_c in simple metals (with s - and p -electrons), because the BCS postulate that the superconducting phenomenon is based on the electron-phonon pairing and based on this¹¹:

$$T_c(P) \propto \sqrt{\frac{k(P)}{M}} \times e^{-\frac{k(P)}{\eta(P)}}, \quad (2)$$

where M is the ion mass, $k(P)$ is pressure dependent lattice spring constant, and $\eta(P)$ is pressure dependent Hopfield parameter⁵⁹ (which is proportional to the electronic density of states and the mean-square electron-phonon matrix element). Due to slow pressure dependence of the $\eta(P)$ in comparison with the $k(P)$ in simple metals, applied pressures cause the suppression of the $T_c(P)$, because of fast suppression of the exponential term in Eq. 2.

The $T_c(P)$ dependences for elements which were metallized under applied pressure (like, sulfur², oxygen⁶⁰, and others^{5,61}) or compounds^{18,62–64} synthesized in the DAC do not cover by universal theory. In each of these cases, first-principles calculations^{30,65–67} are used to predict the $T_c(P)$ relationship that can be compared with experiment.

Here we deduced pressure dependences for the Debye temperature, $\Theta_D(P)$, the electron-phonon coupling constant, $\lambda_{e-ph}(P)$, and the transition temperature, $T_c(P)$, in compressed sulfur. For the latter, we utilized strict resistance criterion^{68–70}:

$$\frac{R(T=T_{c,0.01})}{R_{norm}} = 0.01, \quad (3)$$

where R_{norm} is the resistance at temperature, where the $R(T)$ starts to drop, and the temperature at this drop is T_c^{onset} .

In Figure 5 we showed the $R(T, B = 0, P)$ datasets reported by Wang *et al*¹³ together with fits to the saturated resistance model^{71,72}, which is based on Bloch-Grüneisen^{73,74} equation, and where the Debye temperature, Θ_D , is one of free-fitting parameters^{73–75}:

$$R(T) = \frac{1}{\left(\frac{\theta(T_c^{onset}-T)}{\left(\frac{R_{norm}}{\left(I_0 \left(F \times \left(1 - \frac{T}{T_c^{onset}} \right)^{3/2} \right) \right)^2} \right)} + \theta(T - T_c^{onset}) \times \frac{1}{R_{sat}} + \frac{1}{R_{norm} + A \times \left(\left(\frac{T}{\Theta_D} \right)^N \times \int_0^{\frac{\Theta_D}{T}} \frac{x^N}{(e^x - 1)(1 - e^{-x})} dx - \left(\frac{T_c^{onset}}{\Theta_D} \right)^N \times \int_0^{\frac{\Theta_D}{T_c^{onset}}} \frac{x^N}{(e^x - 1)(1 - e^{-x})} dx \right)} \right)} \quad (4)$$

where $\theta(x)$ is the Heaviside step function, N is the power-law exponent associated with the dominant type of the charge carrier interaction^{75–81} in materials with metallic resistance (where $N = 5$ is associated with the electron-phonon interaction), $I_0(x)$ is the zero-order modified Bessel function of the first kind, and T_c^{onset} , F , Θ_D , R_{norm} , A , R_{sat} are free-fitting parameters.

The term of $\frac{R_{norm}}{\left(I_0 \left(F \times \left(1 - \frac{T}{T_c^{onset}} \right)^{3/2} \right) \right)^2}$ was proposed by Tinkham⁸² (and further modified in Ref.⁸³),

and the term of $\left(\frac{1}{R_{\text{sat}}} + \frac{1}{R_{\text{norm}} + A \times \left(\frac{T}{\Theta_D}\right)^5 \times \int_0^{\frac{\Theta_D}{T}} \frac{x^5}{(e^x - 1)(1 - e^{-x})} dx}\right)$ was proposed by Wiesmann *et al.*⁷². Further

details for the fitting function (Eq. 4) can be found elsewhere^{68,72,81–86}, including our previous studies^{80,83,87} where we analyzed data on highly compressed sulfur S-III phase reported in

Refs.^{2,61}. In Fig. 5 we used the phase identification (i.e., S-III, S-IV, and S-V) based on report by

Degtyareva *et al.*⁸, and other relevant studies^{6,8–10,13,16}.

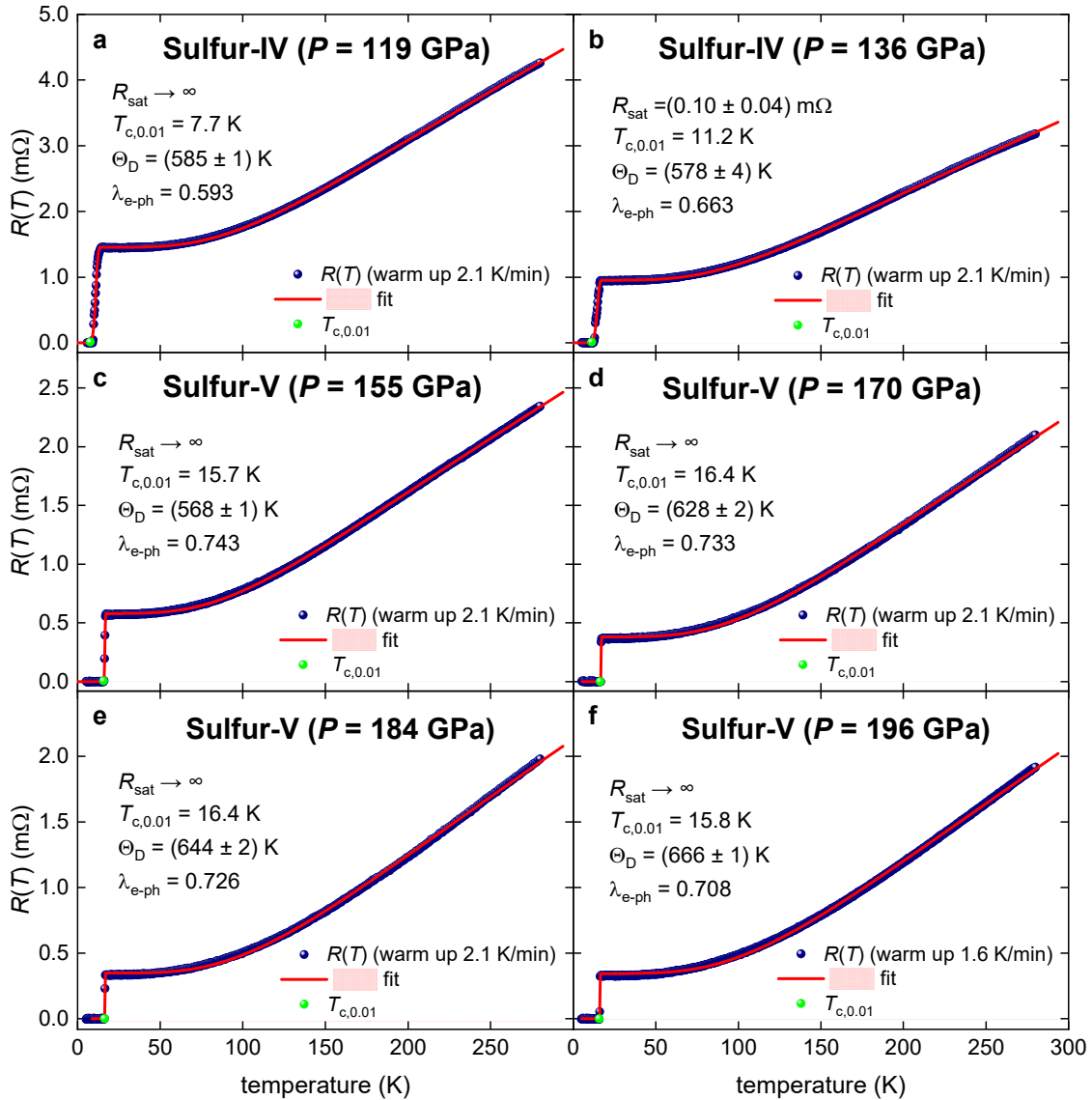


Figure 5. $R(T, B = 0, P)$ in compressed sulfur measured by Wang *et al.*¹³ and data fits to Eq. 4, where $N = 5$ is fixed parameter. Green balls indicate $T_{c,0.01}$. The goodness of fit: (a) 0.9997; (b) 0.9998; (c) 0.99992; (d) 0.9996; (e) 0.9995; (f) 0.9996. The thickness of 95% confidence bands (pink shadow areas) is narrower than the width of the fitting lines.

Deduced Θ_D and $T_{c,0.01}$ were used to determine the electron-phonon coupling constant λ_{e-ph} , which is the root of the system of equations^{68,88,89}:

$$\begin{cases} T_{c,0.01} = \frac{\Theta_D}{1.45} \times e^{-\left(\frac{1.04(1+\lambda_{e-ph})}{\lambda_{e-ph}-\mu^* \times (1+0.62 \times \lambda_{e-ph})}\right)} \times f_1 \times f_2^* \\ f_1 = \left(1 + \left(\frac{\lambda_{e-ph}}{2.46 \times (1+3.8 \times \mu^*)}\right)^{3/2}\right)^{1/3} \\ f_2^* = 1 + (0.0241 - 0.0735 \times \mu^*) \times \lambda_{e-ph}^2 \end{cases} \quad (5)$$

where μ^* is the Coulomb pseudopotential parameter (ranging from $\mu^* = 0.10 - 0.16$ ^{66,90}), for which the mean value of $\mu^* = 0.13$ will be used for compressed sulfur below.

Derived $\Theta_D(P)$, $T_{c,0.01}(P)$, and $\lambda_{e-ph}(P)$ are shown in Fig. 6, where we also showed deduced values for S-III phase from our previous studies^{83,87}. Derived $\lambda_{e-ph}(P \geq 119 \text{ GPa})$ (Figs. 5,6) are in a very good agreement with the value computed by first principles calculations^{7,91}.

There is an immediate conclusion that the phase boundary between phase S-III and S-IV is the range of $110 \text{ GPa} < P < 119 \text{ GPa}$. This can be seen in the $\Theta_D(P)$ and $\lambda_{e-ph}(P)$ dependences, where a remarkably huge break in $\Theta_D(P)$ from $\Theta_D(P = 110 \text{ GPa}) \cong 200 \text{ K}$ and $\Theta_D(P = 119 \text{ GPa}) \cong 600 \text{ K}$ has been revealed.

We determined this phase boundary at $110 \text{ GPa} < P < 119 \text{ GPa}$, which is significantly different from the reported boundary at $P \cong 85 \text{ GPa}$ in Refs.^{8,13}. However, our approach to determine the phase boundary is based on the derivation of the Debye temperature (and the electron-phonon coupling constant), which have a huge (large) change in the pressure range of $110 \text{ GPa} < P < 119 \text{ GPa}$, while the standard approach is based on the change in the slope of lattice parameters variation vs applied pressure and where the change is small^{8,13}.

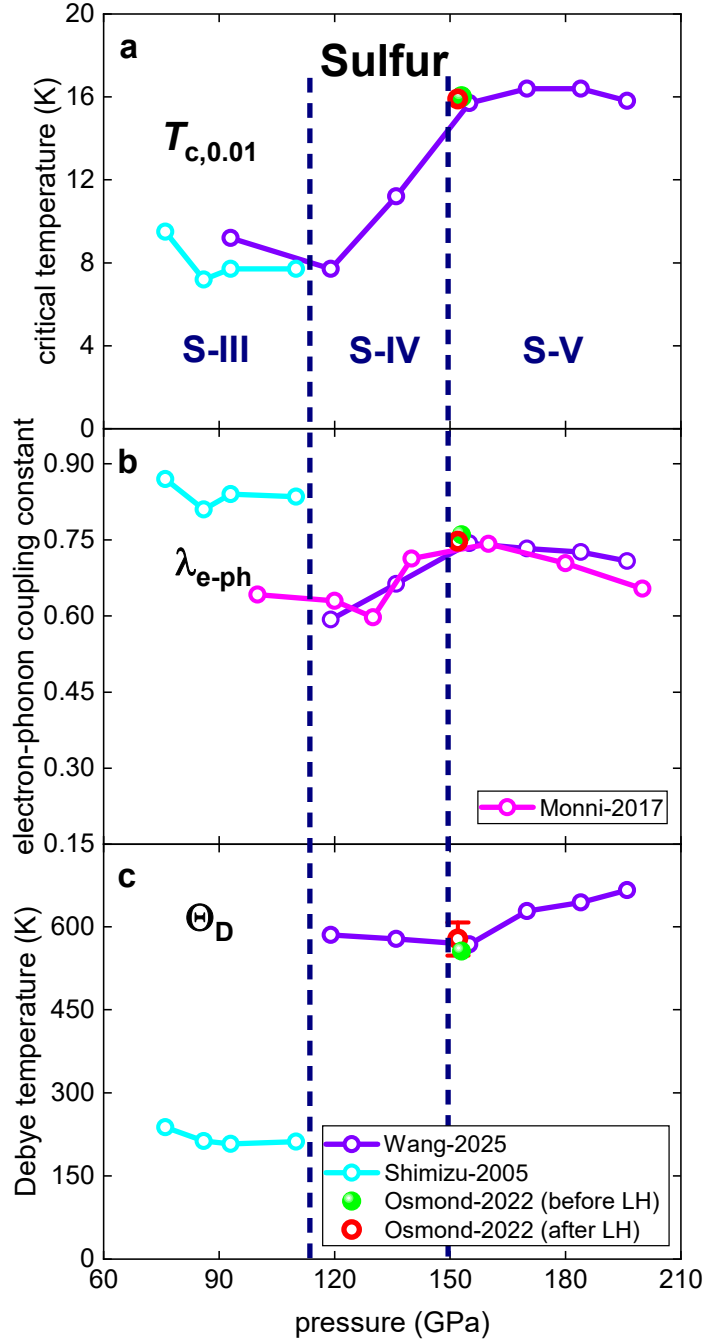


Figure 6. Derived (a) $T_{c,0.01}(P)$, (b) $\lambda_{e-ph}(P)$, and (c) $\Theta_D(P)$ for highly compressed sulfur. Magenta – $\lambda_{e-ph}(P)$ computed by the first-principles calculations by Monni *et al.*⁹¹; cyan – values deduced in Refs.^{83,87} from experimental $R(T, P)$ data reported by Shimizu *et al.*⁵; violet – values deduced herein from experimental $R(T, P)$ data reported by Wang *et al.*¹³; green - value deduced herein from experimental $R(T, P = 153 \text{ GPa})$ data reported by Osmond *et al.*²³ for pure sulfur before the laser heat (LH); red - value deduced herein from experimental $R(T, P = 153 \text{ GPa})$ data reported by Osmond *et al.*²³ for mixture of BH_3NH_3 and sulfur after LH. Phase boundaries are based on Refs.^{5,6,8-10,13,16,23}.

3.4. The upper critical field and the Fermi temperature

Du *et al.*¹² reported the upper critical field data, $B_{c2}(T, P = 160 \text{ GPa})$, which was deduced from measured $\Delta(T, B, P = 160 \text{ GPa})$ dependence, as the field at which the superconducting gap closes. This $B_{c2}(T, P = 160 \text{ GPa})$ dataset is shown in Fig. 7,a together with the fit to the $B_{c2}(T)$ analytical model recently proposed by Prozorov and Kogan⁹²:

$$B_{c2}(T) = \frac{\phi_0}{2\pi\xi^2(0)} \times \left(\frac{1 - \left(\frac{T}{T_c}\right)^2}{1 + 0.42 \times \left(\frac{T}{T_c}\right)^{1.47}} \right), \quad (6)$$

where ϕ_0 is the superconducting magnetic flux quantum, and $\xi(0)$ is the ground state coherence length.

In Fig. 7,b we showed the $B_{c2}(T, P = 163 \text{ GPa})$ dataset which was deduced from the $R(T, B, P = 163 \text{ GPa})$ reported by Wang *et al.*¹³ (in their Fig. 2,b¹³) by applying the criterion described by Eq. 3. The fit of the $B_{c2}(T, P = 163 \text{ GPa})$ to the Eq. 7 is shown in Fig. 7,b.

Deduced $\xi(0)$ values were substituted to the following equation to calculate the Fermi temperature, T_F ^{41,93}:

$$T_F = \frac{\pi^2 m_e}{8 \cdot k_B} \times (1 + \lambda_{e-ph}) \times \xi^2(0) \times \left(\frac{\alpha k_B T_c}{\hbar} \right)^2, \quad (7)$$

where m_e is bare electron mass, \hbar is reduced Planck constant, $\alpha \equiv \frac{2\Delta(0)}{k_B T_c}$ is the gap-to-transition temperature ratio. Other parameters in Eq. 7 were taken from Figs. 1,6. For $B_{c2}(T, P = 163 \text{ GPa})$ data showed in Fig. 7,b, the gap-to-transition temperature ratio $\frac{2\Delta(0)}{k_B T_c}$ was calculated by linear empirical relation proposed in Ref.⁹⁴:

$$\alpha \equiv \frac{2\Delta(0)}{k_B T_c} = 3.26 + 0.74 \times \lambda_{e-ph}, \quad (8)$$

Calculated T_F values are shown in both panels of Fig. 7.

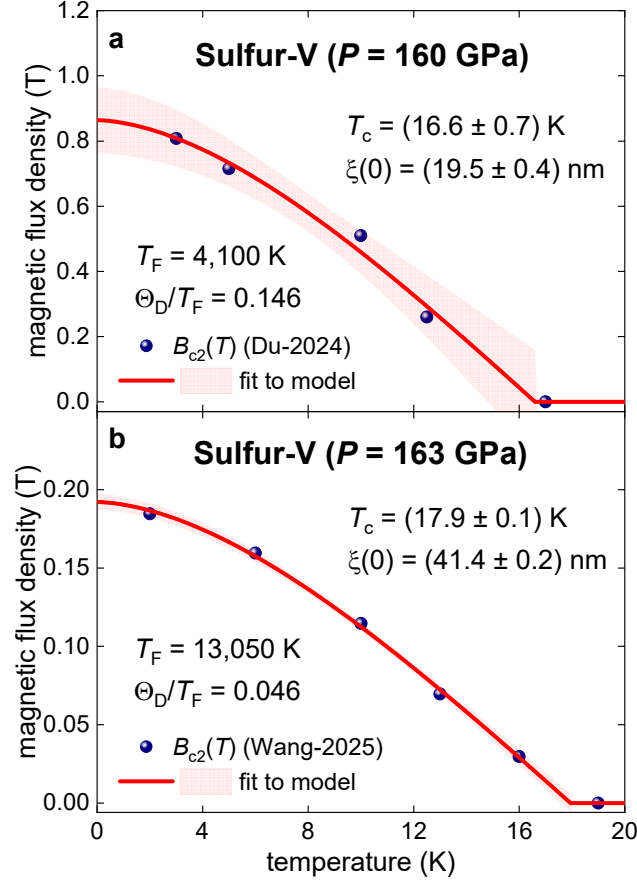


Figure 7. $B_{c2}(T)$ data and fits to to Eq. 6⁹². (a) $B_{c2}(T)$ reported by Du *et al*¹²; and (b) deduced from $R(T, B, P = 163 \text{ GPa})$ data reported by Wang *et al*¹³ by applying criterion of $\frac{R(T=T_{c,0.01})}{R_{norm}} = 0.01$. Fits quality (a) $R = 0.991$; and (b) $R = 0.9992$. Derived parameters are shown. The value of $\Theta_D = 600 \text{ K}$ is assumed.

Deduced Fermi temperature T_F (Fig. 7) was used to locate sulfur-V phase in the Uemura plot^{95,96} (Fig. 8). In the result, it was found that the sulfur phase S-V locates in a close proximity to the sulfur phase S-III for which we deduced T_F in previous study⁸⁷. It can be seen (Fig. 8) that both phases of sulfur are located at the intermediate band between unconventional and BCS bands in the Uemura plot.

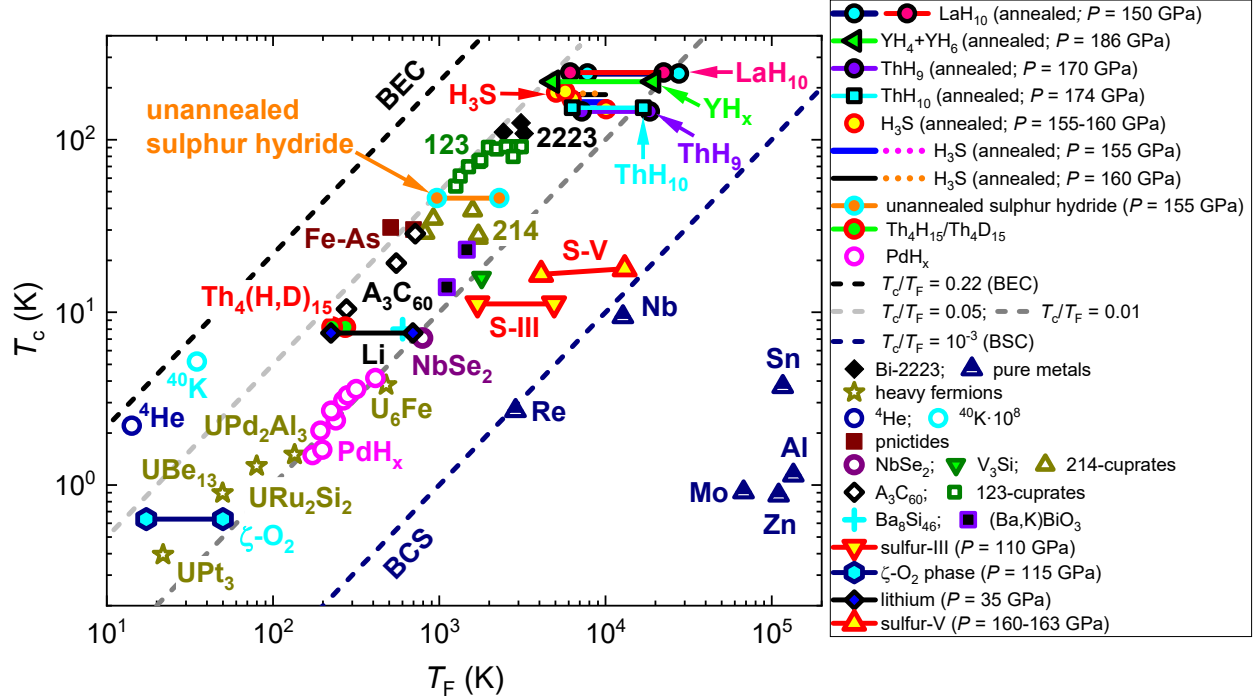


Figure 8. Uemura plot (T_c vs. T_F) where superconducting phases of sulfur (S-III and S-V) are shown together with main superconducting families. References to the original data are in Refs. ^{85,93,97,98}.

We also located S-III and S-V phases in the $\frac{\theta_D}{T_F}$ vs T_c plot (Fig. 9). This type of plot was proposed in Ref.⁹⁷ and it shows that all high- T_c and near-room-temperature superconductors exhibit^{85,97,98} the $\frac{\theta_D}{T_F}$ ratio in the range of $0.04 \leq \frac{\theta_D}{T_F} \leq 0.4$. Both sulfur phases studied herein exhibit the ratio of $\frac{\theta_D}{T_F}$ in this range (Figs. 7,9).

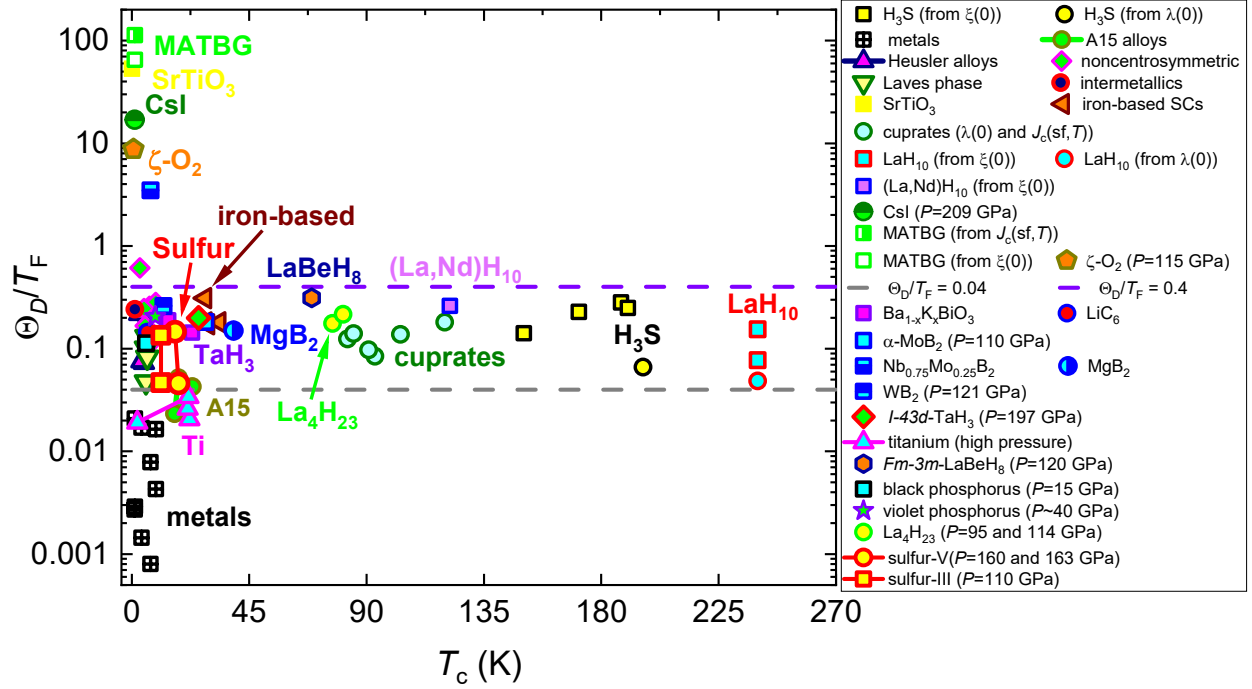


Figure 9. Plot of $\frac{\Theta_D}{T_F}$ vs T_c for main families of superconductors, and where the superconducting phases of sulfur (S-III and S-V) are shown. References to data can be found in Refs.^{41,85,93,97,98}.

3.5. Highly compressed unreacted sulfur in the H_3S+S mixture before laser heating

Considering that sulfur is a starting chemical element for the synthesis of the H_3S and D_3S superconductors^{19,20,22,23,31,32,45}, it is important to analyse available experimental data on unreacted elemental sulfur in the mixture of H_3S , H_3NH_3B , and S in the DAC874 where the H_3S phase is synthesized.

As the first step of this analysis, in Fig. 10 we fitted to Eq. 4 the $R(T, P = 153 \text{ GPa})$ data measured in compressed sulfur before the laser heating (study by Osmond *et al*²³). Deduced $T_{c,0.01}(P)$, $\lambda_{e-ph}(P)$, and $\Theta_D(P)$ from Fig. 10,a are shown in Fig. 6, where one can see excellent agreement between deduced values from raw data reported by two different research groups^{13,23}. It should be also noted that the absolute values of the $R(T, P = 153 \text{ GPa})$ ²³ and $R(T, P = 155 \text{ GPa})$ ¹³ are differed by a factor of ~ 70 . This shows the robustness of our analysis (Eqs. 4,5 and Ref.⁶⁸).

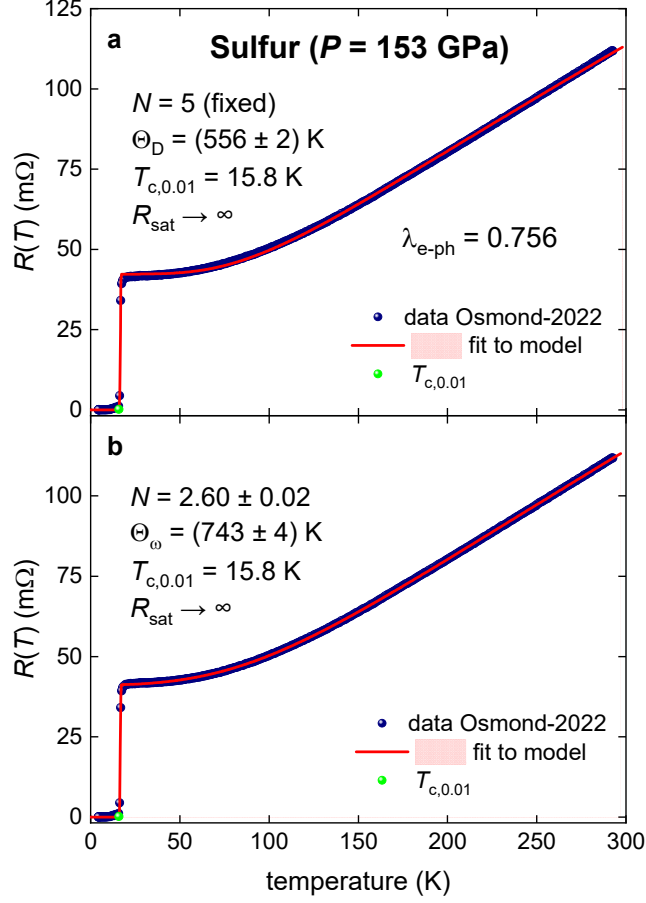


Figure 10. $R(T, B = 0, P = 153 \text{ GPa})$ in compressed sulfur measured by Osmond *et al*¹³ and data fits to Eq. 4, where (a) $N = 5$ (*fixed*) and (b) $N = 2.60 \pm 0.02$ is free-fitting parameter. Deduced parameters are shown. Green balls indicate $T_{c,0.01}$. The goodness of fits: (a) 0.9997 and (b) 0.99997. The thickness of 95% confidence bands (pink shadow areas) is narrower than the width of the fitting lines.

Osmond *et al*²³ also reported that they fitted normal state resistance data $R(T, P = 153 \text{ GPa})$ to the Bloch-Grüneisen equation, where the power-law exponent N was fixed to 3:

$$R(T) = R_{norm} + A \times \left(\frac{T}{\Theta_\omega}\right)^3 \times \int_0^{\frac{\Theta_\omega}{T}} \frac{x^3}{(e^x - 1)(1 - e^{-x})} dx. \quad (9)$$

where Θ_ω is the characteristic temperature associated with the power-law exponent $N = 3$, which differs from the Debye temperature Θ_D which is associated with the electron-phonon scattering and $N = 5$. In the result, Osmond *et al*²³ deduced $\Theta_\omega = 680 \text{ K}$.

In Fig. 10,b we used a different approach^{80,81,86}, which is the data fit to Eq. 4, where N is a free-fitting parameter (this approach was applied earlier⁸⁰ for compressed sulfur at pressures $P =$

76, 86, 93 GPa). Deduced $\Theta_\omega(153 \text{ GPa}) = 743 \pm K$ and $N = 2.60 \pm 0.02$ are close, but not equal to $\Theta_\omega(153 \text{ GPa}) = 680 \text{ K}$ derived at the fixed $N = 3.0$ value (as reported by Osmond *et al*²³). Based on this, there is an interest in revealing the $\Theta_\omega(P)$ and $N(P)$ values for all available $R(T, B = 0, P)$ data for compressed sulfur, which we showed in Figs. 10-12.

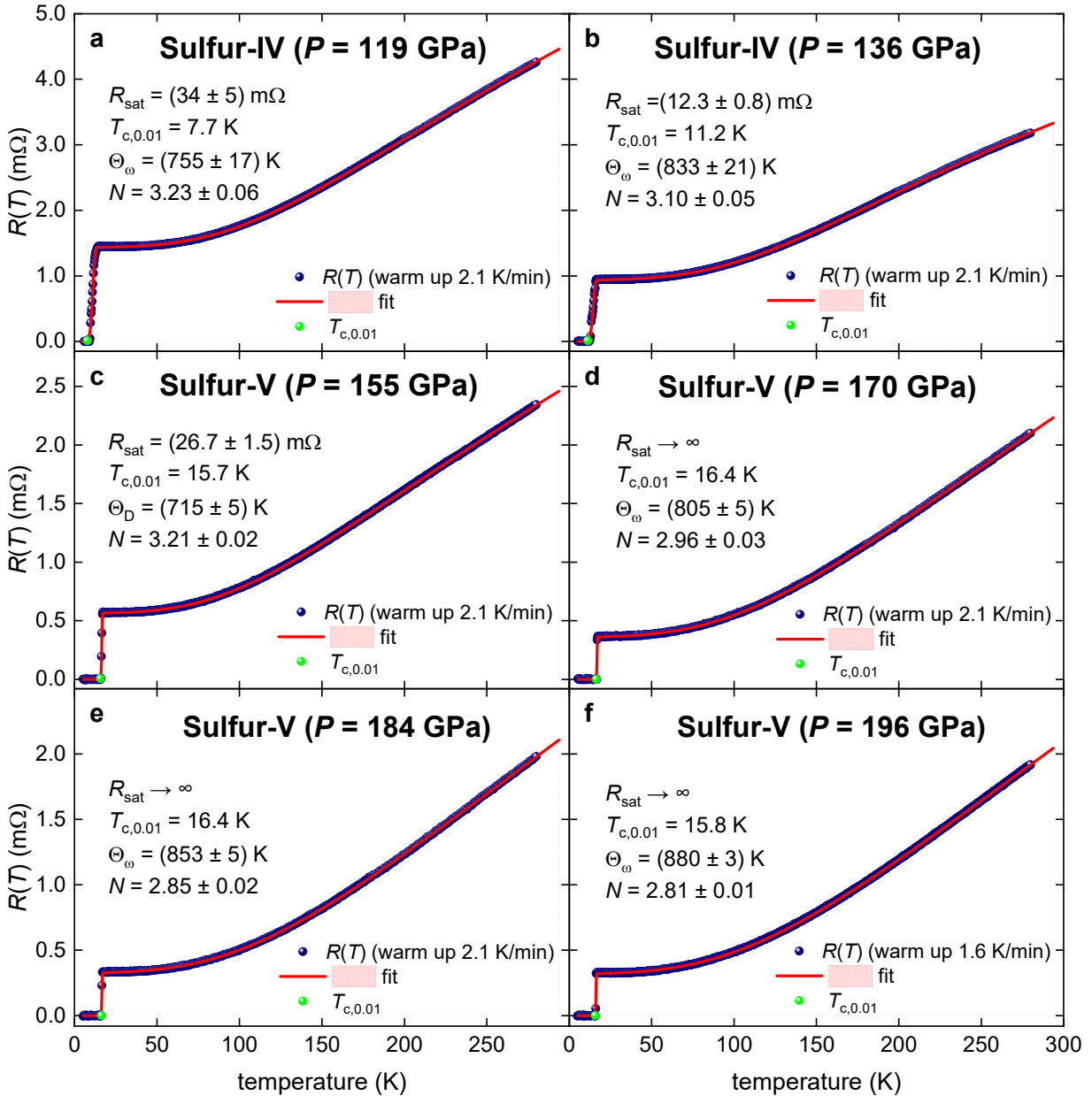


Figure 11. $R(T, B = 0, P)$ of the compressed sulfur measured by Wang *et al*¹³ and data fits to Eq. 4, where N is free-fitting parameter. Green balls indicate $T_{c,0.01}$. The goodness of fit for all panels is better than 0.9998. The thickness of 95% confidence bands (pink shadow areas) is narrower than the width of the fitting lines.

In our earlier study⁸⁰, we already fitted several $R(T, P)$ datasets reported by Shimizu *et al.*^{2,5,61} to Eq. 4, where N is free-fitting parameter, and in Figure 12 we show the fit for the remaining dataset reported in Refs.^{2,5,61}.

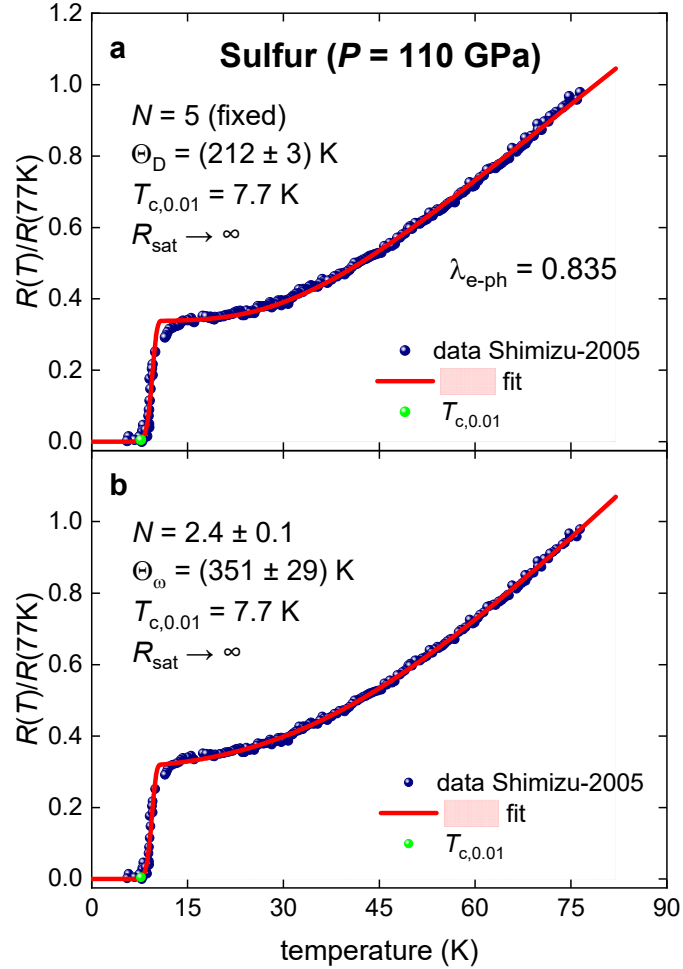


Figure 12. $R(T, B = 0, P = 110 \text{ GPa})$ for compressed sulfur measured by Shimizu *et al.*⁵ and fits to Eq. 4, where N is (a) fixed value ($N = 5$), and (b) is free-fitting parameter. Green balls indicate $T_{c,0.01}$. The goodness of fit (COD) is (a) 0.9972, and (b) 0.9978. The thickness of 95% confidence bands (pink shadow areas) is narrower than the width of the fitting lines.

In Figure 13 we summarized derived $T_c(P)$, $N(P)$, and $\Theta_\omega(P)$ dependences for highly compressed sulfur. Free-fitting power-law exponent is within a range of $2.4 \leq N \leq 3.2$, which is close, but not equal to the $N = 3$.

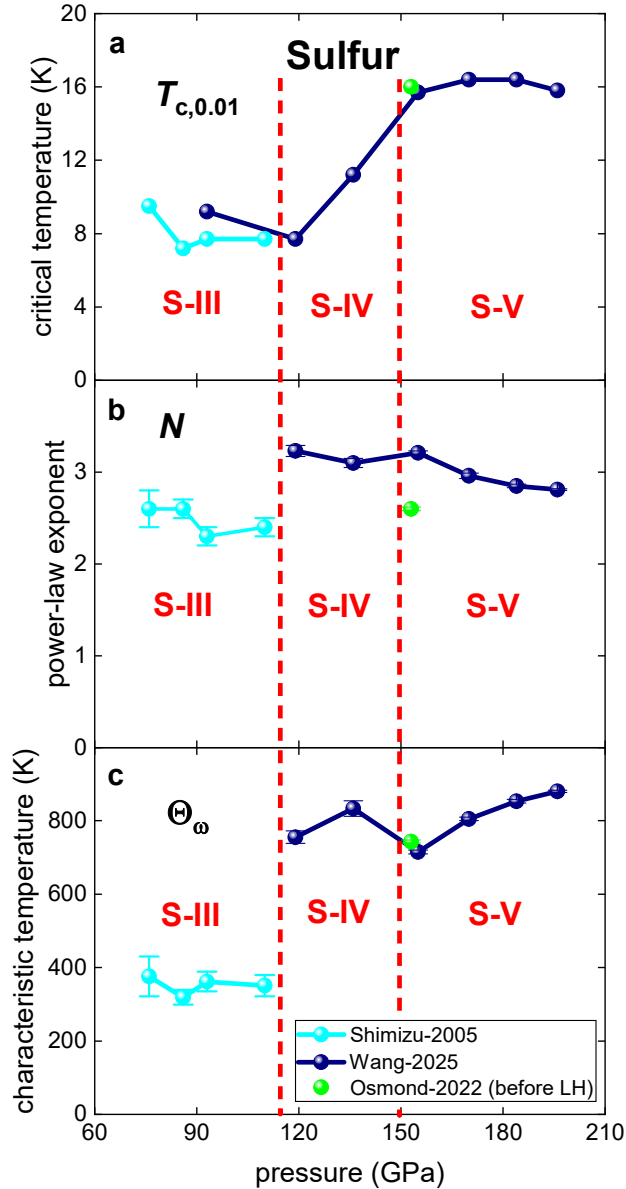


Figure 13. Derived (a) $T_{c,0.01}(P)$, (b) $N(P)$, and (c) $\Theta_{\omega}(P)$ for highly compressed sulfur. cyan – values deduced from experimental $R(T, P)$ data reported by Shimizu *et al.*⁵; navy – values deduced from experimental $R(T, P)$ data reported by Wang *et al.*¹³; green - value deduced herein from experimental $R(T, P = 153 \text{ GPa})$ data reported by Osmond *et al.*^{13,23}. Phase boundaries are based on Refs.^{5,6,8–10,13,16,23}.

3.6. Highly compressed unreacted sulfur in the $\text{H}_3\text{S}+\text{S}$ mixture after laser heat

Osmond *et al.*²³ also reported data for sample contained H_3S and S after the laser heating.

Here is the instrumental broadening function $\beta_i(2\theta)$ in Figure 14, that was determined using X-

ray scanning of a CeO₂ sample. XRD peaks were fitted to Gaussian peak function and obtained $\beta_i(2\theta)$ dataset was fitted to Caglioti equation⁴⁸:

$$\beta_{inst}(2\theta) = \sqrt{U \cdot \tan^2\left(\frac{2\theta}{2}\right) + V \cdot \tan\left(\frac{2\theta}{2}\right) + W}, \quad (10)$$

where U , V , and W are free-fitting parameters. Result of the fit is shown in **Error! Reference source not found.**4, where derived parameters are: $U = 0$ (fixed), $V = 0.0040 \pm 0.0004$, $W = 0.00284 \pm 0.00005$.

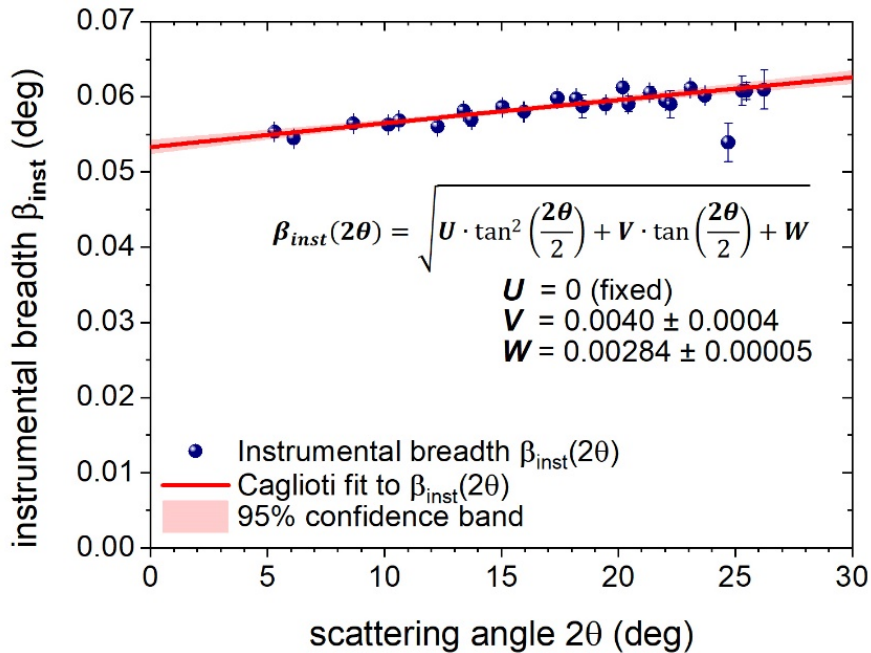


Figure 14. XRD peaks breadth, $\beta_{inst}(2\theta)$, for CeO₂ recorded by Osmond *et al*²³ and the data fit to Caglioti equation (Eq. 10). Error bars are from the Gaussian fitting error. 95% confidence bands are shown by pink areas. Deduced parameters are shown. Fit quality is 0.8418.

In Figure 15, the blue circles indicate the points selected to analyze the strain distribution in sulfur, the original figure from Osmond *et al*²³ is designated there as Fig. 1,c.

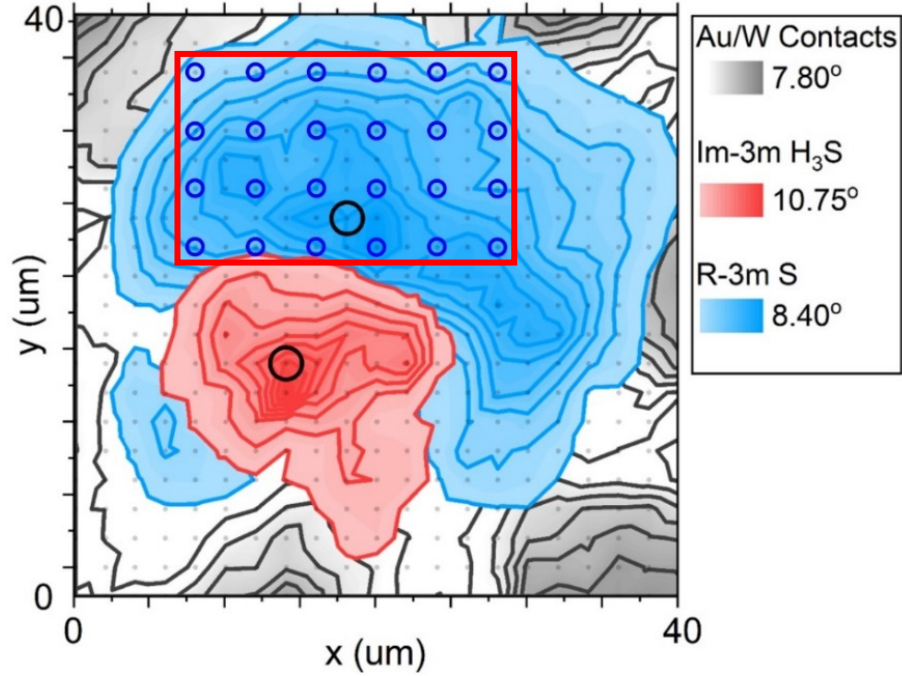


Figure 15. Selected points, depicted by blue circles (circles were shown in the original Figure 1,c from Osmond *et al*²³), for which the size-strain analysis has been performed (XRD data for analysis was reported by Osmond *et al*²³). The original figure from Osmond *et al*²³ is designated there as Fig. 1,c.

XRD peaks of sulfur were fitted to Gaussian peak function, and after the subtraction of the instrumental broadening, the obtained $\beta(\theta)$ dataset was fitted to Williamson-Hall equation⁹⁹:

$$\beta(\theta) = \frac{k_s \times \lambda}{D \cos(\theta)} + 4 \times \varepsilon \times \tan(\theta), \quad (11)$$

where k_s is the Scherrer constant usually assigned as 0.9, $\lambda = 0.2894 \text{ \AA}$ is the wavelength of the X-ray radiation used in Ref.²³, and D is the mean size of nanocrystallines, and the ε is the nanocrystalline strain.

Some of these fits are shown in Fig. 16. In the result, we found that the sulfur in the mixture of H₃S+S in the DAC after laser heating has larger crystal size, D , which exceeds the resolution of the diffractometer (i.e. $D > 25 \text{ nm}$) and, thus, we revealed the sulfur strain map.

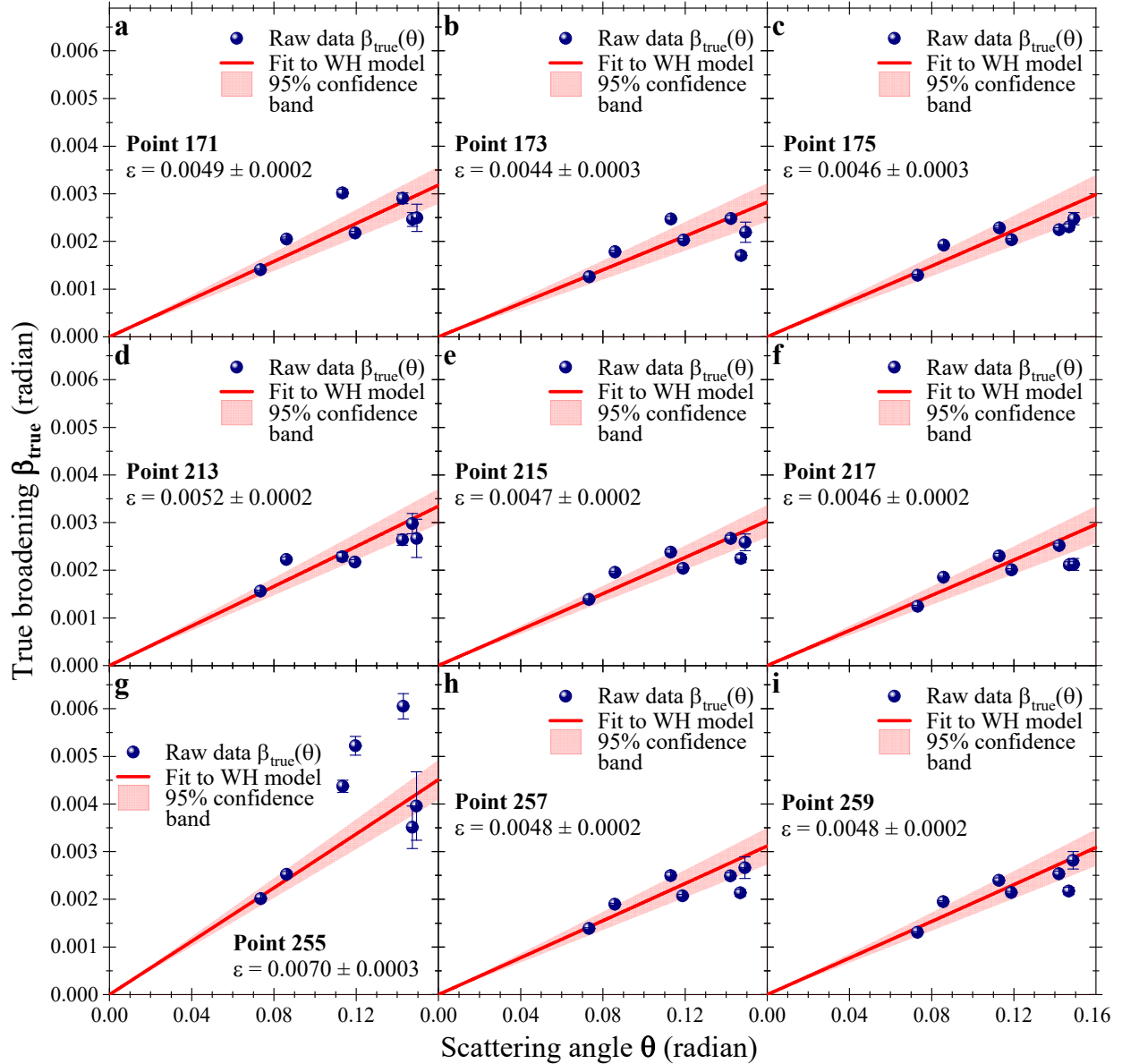


Figure 16. Several Williamson-Hall plots for mapping of strain $\varepsilon(x,y)$ in sulfur region, marked by red frame in Fig. 15. Point designation is as it uses by Osmond *et al*²³ in their raw data files.

Figure 16 shows spatial maps of 8.4° sulfur XRD peak intensity and strain $\varepsilon(x,y)$ in sulfur region, marked by red frame in Fig. 15, where X and Y coordinates correspond to both in Fig. 15. The strain is ranges from $\varepsilon = 0.0045$ to 0.0070 across analyzed area, where in the central region the strain is within a range of $\varepsilon = (0.40-0.50) \%$. The comparing the two maps (showed in two panels of Fig. 17) it can be seen that areas of low sulfur peak intensity correlate with higher

microstrain values. At the same time, the obtained values of microstrain in this experiment remain relatively low.

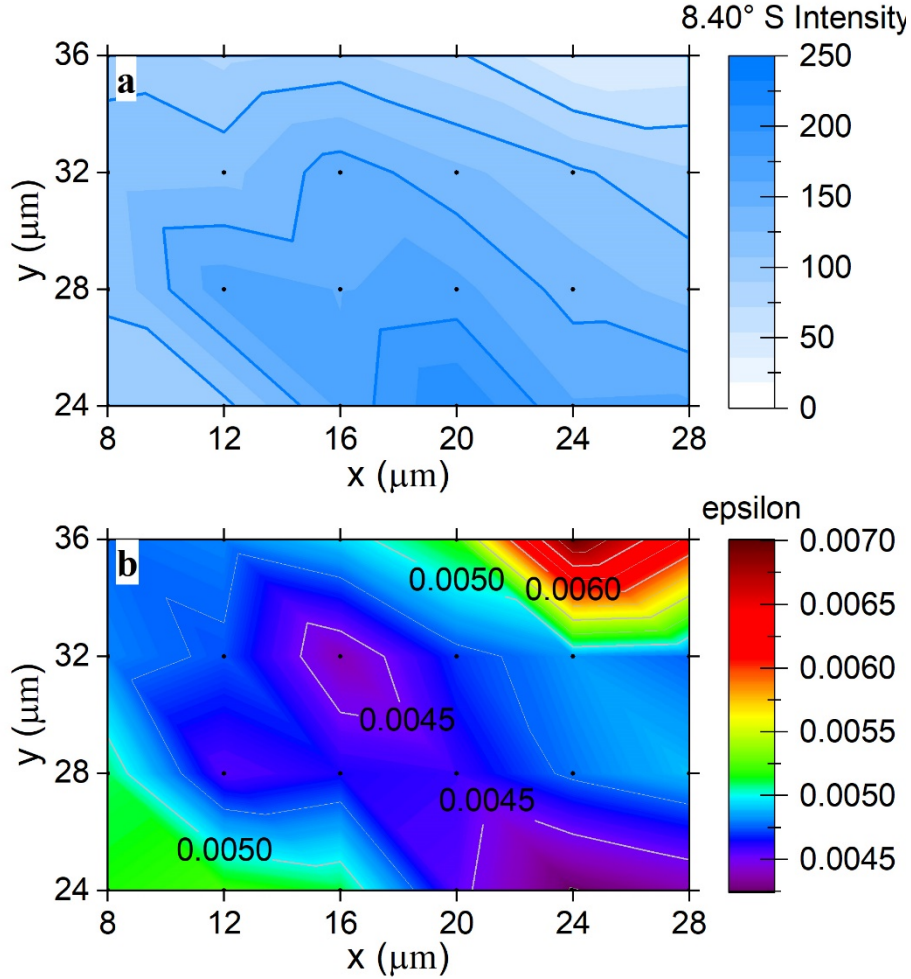


Figure 17. Spatial mapping of strain $\varepsilon(x,y)$ in sulfur region, marked by red frame in Fig. 15. X and Y coordinates correspond to both in Fig. 15: (a) intensity map of 8.4° sulfur XRD peak; (b) the $\varepsilon(x,y)$ map for sulfur extracted from XRD data reported by Osmond *et al*²³.

Osmond *et al*²³ also reported two $R(T, P = 153 \text{ GPa})$ curves measured on samples with synthesized H_3S and remaining sulfur (after the laser heating of the mixture of the BH_3NH_3 and sulfur). In Figure 18, we showed the reported $R(T, P = 153 \text{ GPa})$ datasets together with the fits to serial two-phase model which we also proposed herein:

$$R_{total}(T, P) = R_{sulfur}(T, P) + R_{\text{H}_3\text{S}}(T, P) \quad (12)$$

where each $R_{phase}(T, P)$ is described by Eq. 4 with independent parameters (i.e., T_c^{onset} , Θ_D , etc.), and where we restricted the model to Bloch-Grüneisen^{73,74} approach with $N = 5$.

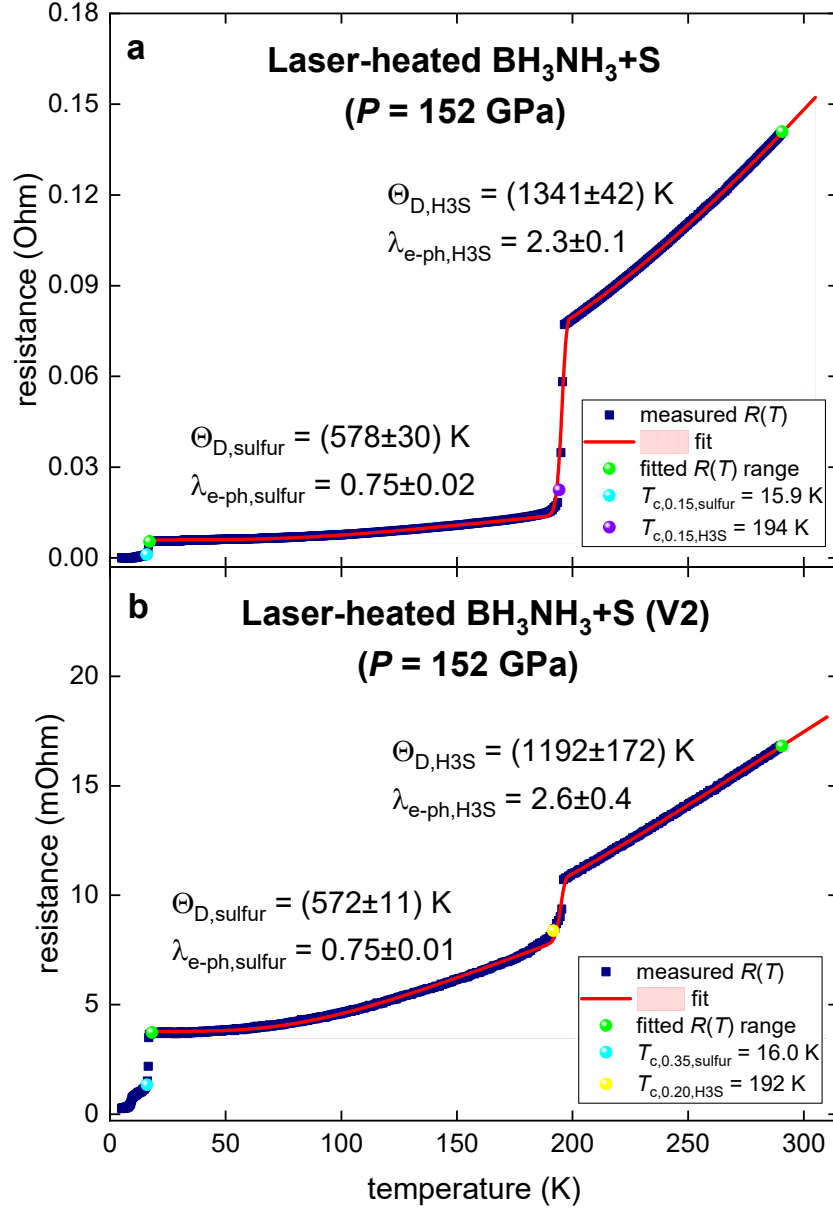


Figure 18. $R(T, P = 152 \text{ GPa})$ for two samples of H₃S+S after laser heat (raw data reported by Osmond *et al*²³) and fits to Eq. 12, where $N = 5$. Deduced parameters are shown in each panel. Green balls in both panels indicate $R(T, P)$ range used for fit. (a) Cyan ball indicates $T_{c,0.15}$ for sulfur; violet ball indicates $T_{c,0.15}$ for H₃S. (b) Cyan ball indicates $T_{c,0.35}$ for sulfur; violet ball indicates $T_{c,0.35}$ for H₃S. The goodness of fit (COD) is (a) 0.9996, and (b) 0.9985. The thickness of 95% confidence bands (pink shadow areas) is narrower than the width of the fitting lines.

It should be stressed, that $\Theta_{D,sulfur}(P = 152 \text{ GPa})$ and $\lambda_{e-ph,sulfur}(P = 152 \text{ GPa})$ deduced for the mixture of $\text{H}_3\text{S}+\text{S}$ phases (after the laser heat of BH_3NH_3 and S precursors) are in excellent agreement with the respectful values derived for pure elemental sulfur (Fig. 6).

Determined $\Theta_{D,H_3S}(P = 152 \text{ GPa})$ and $\lambda_{e-ph,H_3S}(P = 152 \text{ GPa})$ are also in excellent agreement with values extracted from the $R(T, P)$ measured in sample with pure H_3S phase^{68,83}, as well as computed by the first-principles calculations^{29,30,35,43,100}.

3.7. Size-strain relation in fast ramp compressed polymeric sulfur

For the completeness of the overview of current status of high-pressure studies of sulfur, in Figure 19 we showed the Williamson-Hall plot for polymeric sulfur synthesized by fast ramp pressure technique to $P = 4.1 \text{ GPa}$ (XRD scan reported by Shi *et al.*¹⁴ (XRD scan approximation by Gaussian peak functions is shown in Fig. 18,a).

Deduced size $D = (7.5 \pm 0.5 \text{ \AA})$ and strain $\varepsilon = (0.03 \pm 0.01)$ should be associated with the cross-section of sulfur chains bundle. Considering that S-S distance in all sulfur phases is about¹⁰¹ $\sim 2.1 \text{ \AA}$, and assuming that angle between sulfur atoms in the chains is ~ 120 degree, we can estimate that each bundle consists of $\frac{\pi}{4} \times \left(\frac{7.5 \text{ \AA}}{2.1 \text{ \AA} \times \sin(30^\circ)} \right)^2 \cong 40 \text{ chains}$. These chains are in strong distorted form, which can be proved by high level of strain, $\varepsilon = (3 \pm 1)\%$.

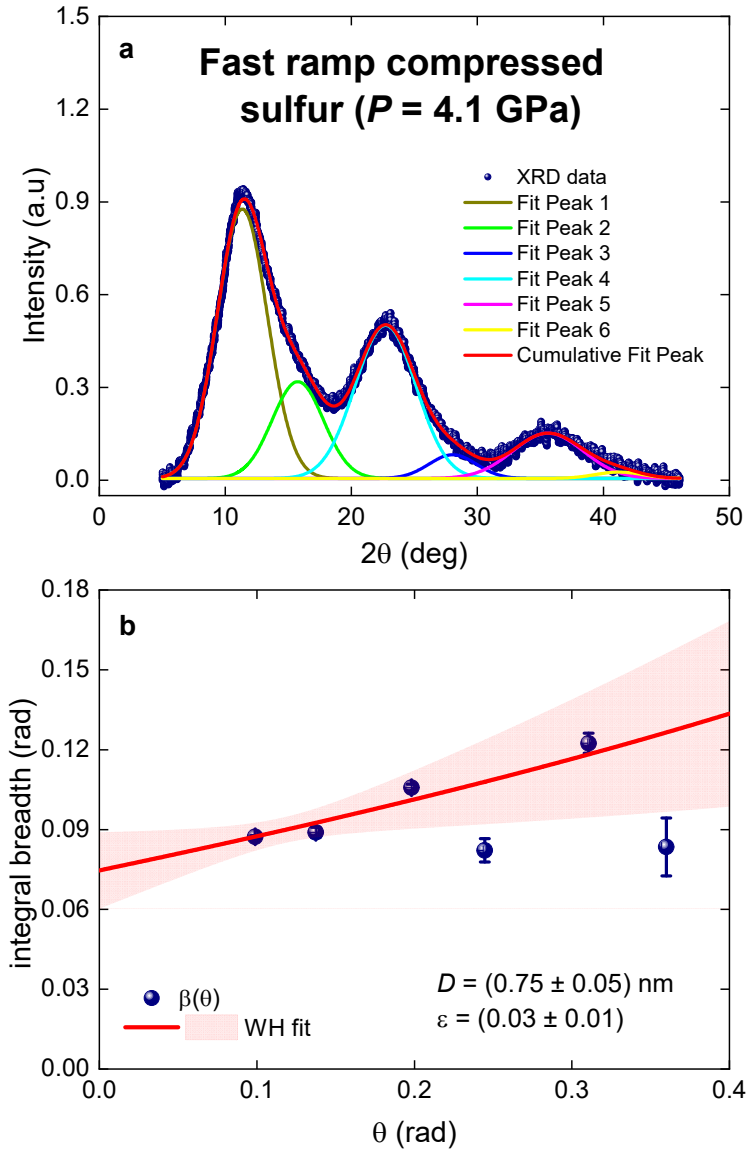


Figure 19. (a) XRD scan (data reported by Shi *et al.*¹⁴) for fast ramp compressed sulfur to $P = 4.1$ GPa and data approximation by Gaussian peak function. (b) Williamson-Hall plot for data presented in panel (a). The goodness of fit (R-squared COD) for (b) is 0.743. 95% confidence bands are shown by pink shadow area.

4. Conclusions

In this study we analyzed recently reported data on compressed sulfur^{12–14,23}. The interest to this nonmetallic element, which has very versatile phase diagram^{52,101}, and which is converting

to superconductor at high pressure, is remaining over the last five decades. Our main findings are:

1. Sulfur at $P = 160 \text{ GPa}$ has the relative jump of the specific heat at transition temperature

$$\frac{\Delta C_{el}}{\gamma T_c} = 1.8 \pm 0.1, \text{ which is in a good agreement with reported}^{12} \text{ experimental value for the ratio}$$

$$\frac{2\Delta(0)}{k_B T_c} = 3.89 \pm 0.06.$$

2. Highly compressed sulfur in its elemental form and being compressed and laser heated in the mixture of H_3S and S , has practically identical Debye temperature, $\Theta_D(P)$, and the electron-phonon coupling constant $\lambda_{e-ph}(P)$.

3. Highly compressed sulfur-III and sulfur-V phases are in the intermediate band between conventional and unconventional superconductors in the Uemura plot. These phases have intermediate strength of the nonadiabaticity, i.e. $0.046 \leq \frac{\Theta_D}{T_F} \leq 0.2$, which is similar to MgB_2 , pnictides, cuprates, La_4H_{23} , ThH_9 , H_3S , LaBeH_8 , and LaH_{10} .

4. Compressed superconducting sulfur in the mixture of H_3S and S has low level of microstrain $\varepsilon \cong 0.5\%$, and high level of microstrain $\varepsilon \cong 3\%$ in the form of molecular chains fabricated by fast ramp compression.

Acknowledgements

The work was carried out within the framework of the state assignment of the Ministry of Science and Higher Education of the Russian Federation for the IMP UB RAS. E.F.T. gratefully acknowledge the research funding from the Ministry of Science and Higher Education of the Russian Federation under Ural Federal University Program of Development within the Priority-2030 Program.

Conflict of interest

The authors declared that they do not have any conflict of interest.

Author contributions

E.F.T. conceived the work. E.G.V.-Z. performed XRD data analysis. E.F.T. performed data analysis for resistance, upper critical field, and superconducting gap. E.F.T. wrote the manuscript with contributions from E.G.V.-Z.

References

1. Yakovlev E N, Stepanov G N, Timofeev Y A & Vinogradov B V. Superconductivity of sulfur at high pressures. *JETP Lett* **28**, 340–342 (1978).
2. Kometani, S., Eremets, M. I., Shimizu, K., Kobayashi, M. & Amaya, K. Observation of Pressure-Induced Superconductivity of Sulfur. *J Physical Soc Japan* **66**, 2564–2565 (1997).
3. Struzhkin, V. V., Hemley, R. J., Mao, H. & Timofeev, Y. A. Superconductivity at 10–17 K in compressed sulphur. *Nature* **390**, 382–384 (1997).
4. Zakharov, O. & Cohen, M. L. Theory of structural, electronic, vibrational, and superconducting properties of high-pressure phases of sulfur. *Phys Rev B* **52**, 12572–12578 (1995).
5. Shimizu, K., Amaya, K. & Suzuki, N. Pressure-induced Superconductivity in Elemental Materials. *J Physical Soc Japan* **74**, 1345–1357 (2005).
6. Luo, H., Greene, R. G. & Ruoff, A. L. β -Po phase of sulfur at 162 GPa: X-ray diffraction study to 212 GPa. *Phys Rev Lett* **71**, 2943–2946 (1993).
7. Whaley-Baldwin, J., Hutcheon, M. & Pickard, C. J. Superconducting incommensurate host-guest phases in compressed elemental sulfur. *Phys Rev B* **103**, 214111 (2021).
8. Degtyareva, O., Gregoryanz, E., Mao, H. K. & Hemley, R. J. Crystal structure of sulfur and selenium at pressures up to 160 GPa. *High Press Res* **25**, 17–33 (2005).
9. Hejny, C., Lundegaard, L. F., Falconi, S., McMahon, M. I. & Hanfland, M. Incommensurate sulfur above $>100</math> GPa. *Phys Rev B* **71**, 020101 (2005).$

10. Degtyareva, O. *et al.* Competition of Charge-Density Waves and Superconductivity in Sulfur. *Phys Rev Lett* **99**, 155505 (2007).
11. Schilling, J. S. & Hamlin, J. J. Recent studies in superconductivity at extreme pressures. *J Phys Conf Ser* **121**, 052006 (2008).
12. Du, F. *et al.* Tunneling Spectroscopy at Megabar Pressures: Determination of the Superconducting Gap in Sulfur. *Phys Rev Lett* **133**, 036002 (2024).
13. Wang, K. *et al.* Evidence for a metal–bosonic insulator–superconductor transition in compressed sulfur. *Proceedings of the National Academy of Sciences* **122**, (2025).
14. Shi, K. *et al.* Sulfur chains glass formed by fast compression. *Nat Commun* **16**, 357 (2025).
15. Moulding, O. *et al.* Mutual stabilization of charge-density-wave and monoclinic distortion in sulfur at high pressures. *Phys Rev Res* **5**, 043188 (2023).
16. Gregoryanz, E. *et al.* Superconductivity in the chalcogens up to multimegabar pressures. *Phys Rev B* **65**, 064504 (2002).
17. Brazhkin, V. V., Voloshin, R. N., Popova, S. V. & Umnov, A. G. Nonmetal-metal transition in sulphur melt under high pressure. *Phys Lett A* **154**, 413–415 (1991).
18. Drozdov, A. P., Erements, M. I., Troyan, I. A., Ksenofontov, V. & Shylin, S. I. Conventional superconductivity at 203 kelvin at high pressures in the sulfur hydride system. *Nature* **525**, 73–76 (2015).
19. Mozaffari, S. *et al.* Superconducting phase diagram of H₃S under high magnetic fields. *Nat Commun* **10**, 2522 (2019).
20. Minkov, V. S., Prakapenka, V. B., Greenberg, E. & Erements, M. I. A Boosted Critical Temperature of 166 K in Superconducting D₃S Synthesized from Elemental Sulfur and Hydrogen. *Angewandte Chemie* **132**, 19132–19136 (2020).
21. Minkov, V. S. *et al.* Magnetic field screening in hydrogen-rich high-temperature superconductors. *Nat Commun* **13**, 3194 (2022).
22. Nakao, H. *et al.* Superconductivity of Pure H₃S Synthesized from Elemental Sulfur and Hydrogen. *J Physical Soc Japan* **88**, 123701 (2019).
23. Osmond, I. *et al.* Clean-limit superconductivity in H_3S synthesized from sulfur and hydrogen donor ammonia borane. *Phys Rev B* **105**, L220502 (2022).
24. Minkov, V. S., Ksenofontov, V., Bud'ko, S. L., Talantsev, E. F. & Erements, M. I. Magnetic flux trapping in hydrogen-rich high-temperature superconductors. *Nat Phys* **19**, 1293–1300 (2023).
25. Szczyński, R. & Durajski, A. P. Unusual sulfur isotope effect and extremely high critical temperature in H₃S superconductor. *Sci Rep* **8**, 6037 (2018).

26. Pinsook, U. & Tanthum, P. Universal resistivity from electron-phonon interaction based on Einstein model: Application to near-room temperature superconductors. *Next Materials* **6**, 100302 (2025).
27. Bondarenko, S. I., Timofeev, V. P., Koverya, V. P. & Krevsun, A. V. Hydrogen in superconductors. (2024).
28. Talantsev, E. F. Unconventional superconductivity in highly-compressed unannealed sulphur hydride. *Results Phys* **16**, 102993 (2020).
29. Errea, I. *et al.* Quantum hydrogen-bond symmetrization in the superconducting hydrogen sulfide system. *Nature* **532**, 81–84 (2016).
30. Errea, I. *et al.* High-Pressure Hydrogen Sulfide from First Principles: A Strongly Anharmonic Phonon-Mediated Superconductor. *Phys Rev Lett* **114**, 157004 (2015).
31. Huang, X. *et al.* High-temperature superconductivity in sulfur hydride evidenced by alternating-current magnetic susceptibility. *Natl Sci Rev* **6**, 713–718 (2019).
32. Matsumoto, R. *et al.* Electrical transport measurements for superconducting sulfur hydrides using boron-doped diamond electrodes on beveled diamond anvil. *Supercond Sci Technol* **33**, 124005 (2020).
33. Zhang, K. *et al.* High-pressure synthesis of a ternary yttrium-sulfur hydride superconductor with a high T_c of approximately 235 K. *Sci China Phys Mech Astron* **67**, 238211 (2024).
34. Du, M., Zhao, W., Cui, T. & Duan, D. Compressed superhydrides: the road to room temperature superconductivity. *Journal of Physics: Condensed Matter* **34**, 173001 (2022).
35. Duan, D. *et al.* Pressure-induced metallization of dense (H₂S)₂H₂ with high- T_c superconductivity. *Sci Rep* **4**, 6968 (2014).
36. Li, Y., Hao, J., Liu, H., Li, Y. & Ma, Y. The metallization and superconductivity of dense hydrogen sulfide. *J Chem Phys* **140**, (2014).
37. Cappelluti, E., Grimaldi, C. & Pietronero, L. Electron–phonon driven unconventional superconductivity: The role of small Fermi energies and of nonadiabatic processes. *Physica C: Superconductivity and its Applications* **613**, 1354343 (2023).
38. Pietronero, L., Boeri, L., Cappelluti, E. & Ortenzi, L. Conventional/unconventional superconductivity in high-pressure hydrides and beyond: insights from theory and perspectives. *Quantum Studies: Mathematics and Foundations* **5**, 5–21 (2018).
39. L. Pietronero, L. Boeri, E. Cappelluti & L. Ortenzi. Conventional/Unconventional superconductivity in high pressure hydrides and beyond: Insights from theory and perspectives. in *2nd International Workshop ‘Towards Room Temperature Superconductivity: Superhydrides and More.’ In Recognition of Professor Vitaly Ginzburg.* (eds. Organizers: *et al.*) (Orange, CA, USA, 2017).
40. Wang, T. *et al.* Absence of conventional room-temperature superconductivity at high pressure in carbon-doped H₃S. *Phys Rev B* **104**, 064510 (2021).

41. Talantsev, E. F. Classifying superconductivity in compressed H3S. *Modern Physics Letters B* **33**, 1950195 (2019).
42. Tallon, J. L. & Talantsev, E. F. Compressed H3S, superfluid density and the quest for room-temperature superconductivity. *J Supercond Nov Magn* **31**, 619–624 (2018).
43. Lilia, B. *et al.* The 2021 room-temperature superconductivity roadmap. *Journal of Physics: Condensed Matter* **34**, 183002 (2022).
44. Einaga, M. *et al.* Crystal structure of the superconducting phase of sulfur hydride. *Nat Phys* **12**, 835–838 (2016).
45. Capitani, F. *et al.* Spectroscopic evidence of a new energy scale for superconductivity in H3S. *Nat Phys* **13**, 859–863 (2017).
46. Shimizu, K. *et al.* Superconductivity and structural studies of highly compressed hydrogen sulfide. *Physica C: Superconductivity and its Applications* **552**, 27–29 (2018).
47. Prescher, C. & Prakapenka, V. B. *DIOPTAS* : a program for reduction of two-dimensional X-ray diffraction data and data exploration. *High Press Res* **35**, 223–230 (2015).
48. Gross-Alltag, F., Chandrasekhar, B. S., Einzel, D., Hirschfeld, P. J. & Andres, K. London field penetration in heavy fermion superconductors. *Zeitschrift für Physik B Condensed Matter* **82**, 243–255 (1991).
49. Gross, F. *et al.* Anomalous temperature dependence of the magnetic field penetration depth in superconducting UBe13. *Zeitschrift für Physik B Condensed Matter* **64**, 175–188 (1986).
50. Bardeen, J., Cooper, L. N. & Schrieffer, J. R. Theory of Superconductivity. *Physical Review* **108**, 1175–1204 (1957).
51. Carbotte, J. P. Properties of boson-exchange superconductors. *Rev Mod Phys* **62**, 1027–1157 (1990).
52. Steudel, R. & Eckert, B. Solid Sulfur Allotropes. in 1–80 (2003). doi:10.1007/b121110.
53. Ma, C. *et al.* Synthesis of medium-entropy alloy superhydride $\text{LaCe}_{10}\text{H}_x$ with high-temperature superconductivity under high pressure. *Phys Rev B* **111**, 024505 (2025).
54. Kharal, G., Chavez, B. L., Huang, S., Jin, R. & Wu, Y. Evolution of the surface phase transitions in IrTe2. *Sci Rep* **14**, 24857 (2024).
55. Fang, A. F., Xu, G., Dong, T., Zheng, P. & Wang, N. L. Structural phase transition in IrTe2: A combined study of optical spectroscopy and band structure calculations. *Sci Rep* **3**, 1153 (2013).
56. You, J. S. *et al.* Thermoelectric properties of the stripe-charge ordering phases in IrTe_2 . *Phys Rev B* **103**, 045102 (2021).

57. Park, S. *et al.* Superconductivity emerging from a stripe charge order in IrTe₂ nanoflakes. *Nat Commun* **12**, 3157 (2021).
58. Deng, L. *et al.* Creation, stabilization, and study at ambient pressure of pressure-induced superconductivity in Bi_{0.5}Sb_{1.5}Te₃. (2025).
59. Hopfield, J. J. On the systematics of high T_c in transition metal materials. *Physica* **55**, 41–49 (1971).
60. Shimizu, K., Suhara, K., Ikumo, M., Eremets, M. I. & Amaya, K. Superconductivity in oxygen. *Nature* **393**, 767–769 (1998).
61. Shimizu, K. Superconducting elements under high pressure. *Physica C: Superconductivity and its Applications* **552**, 30–33 (2018).
62. Eremets, M. I., Minkov, V. S., Drozdov, A. P. & Kong, P. P. The characterization of superconductivity under high pressure. *Nat Mater* **23**, 26–27 (2024).
63. Drozdov, A. P. *et al.* Superconductivity at 250 K in lanthanum hydride under high pressures. *Nature* **569**, 528–531 (2019).
64. Kong, P. *et al.* Superconductivity up to 243 K in the yttrium-hydrogen system under high pressure. *Nat Commun* **12**, 5075 (2021).
65. Hou, P., Belli, F., Bianco, R. & Errea, I. Strong anharmonic and quantum effects in Pm₃⁻ⁿ AlH₃ under high pressure: A first-principles stud. *Phys Rev B* **103**, 134305 (2021).
66. Semenok, D. Computational design of new superconducting materials and their targeted experimental synthesis. *PhD Thesis; Skolkovo Institute of Science and Technology* (2023) doi:10.13140/RG.2.2.28212.12161.
67. Troyan, I. A., Semenok, D. V., Sadakov, A. V., Lyubutin, I. S. & Pudalov, V. M. PROGRESS, PROBLEMY I PERSPEKTIVY KOMNATNO-TEMPERATURNNOY SVERKhPROVODIMOSTI. *Журнал экспериментальной и теоретической физики* **166**, (2024).
68. Talantsev, E. F. Advanced McMillan’s equation and its application for the analysis of highly-compressed superconductors. *Supercond Sci Technol* **33**, 094009 (2020).
69. Talantsev, E. Two-Band Superconductivity and Transition Temperature Limited by Thermal Fluctuations in Ambient Pressure La_{3-x}Pr_xNi₂O_{7-δ} (x = 0.0, 0.15, 1.0) Thin Films. (2025) doi:10.20944/preprints202502.0137.v2.
70. Talantsev, E. F. Quantifying interaction mechanism in infinite layer nickelate superconductors. *J Appl Phys* **134**, (2023).
71. Fisk, Z. & Webb, G. W. Saturation of the High-Temperature Normal-State Electrical Resistivity of Superconductors. *Phys Rev Lett* **36**, 1084–1086 (1976).
72. Wiesmann, H. *et al.* Simple Model for Characterizing the Electrical Resistivity in ρ_{xx} Superconductors. *Phys Rev Lett* **38**, 782–785 (1977).

73. Bloch, F. Zum elektrischen Widerstandsgesetz bei tiefen Temperaturen. *Zeitschrift für Physik* **59**, 208–214 (1930).
74. Grüneisen, E. Die Abhängigkeit des elektrischen Widerstandes reiner Metalle von der Temperatur. *Ann Phys* **408**, 530–540 (1933).
75. Jayakumar, A., Dixit, V., Jose, S., Kamble, V. B. & Jaiswal-Nagar, D. Charge transport variation from Bloch–Grüneisen to Mott variable range hopping and transport change due to hydrogenation in Palladium thin films. *Sci Rep* **11**, 22298 (2021).
76. Jiang, H. *et al.* Physical properties and electronic structure of $\text{Sr}_{2-x}\text{Cr}_3\text{As}_2\text{O}_{10}$ containing CrO_2 and Cr_2As_2 square-planar lattices. *Phys Rev B* **92**, 205107 (2015).
77. Electrical and thermal resistivity of the transition elements at low temperatures. *Philosophical Transactions of the Royal Society of London. Series A, Mathematical and Physical Sciences* **251**, 273–302 (1959).
78. Poker, D. B. & Klabunde, C. E. Temperature dependence of electrical resistivity of vanadium, platinum, and copper. *Phys Rev B* **26**, 7012–7014 (1982).
79. Matula, R. A. Electrical resistivity of copper, gold, palladium, and silver. *J Phys Chem Ref Data* **8**, 1147–1298 (1979).
80. Talantsev, E. Classifying Charge Carrier Interaction in Highly Compressed Elements and Silane. *Materials* **14**, 4322 (2021).
81. Talantsev, E. F. The dominance of non-electron–phonon charge carrier interaction in highly-compressed superhydrides. *Supercond Sci Technol* **34**, 115001 (2021).
82. Tinkham, M. Resistive Transition of High-Temperature Superconductors. *Phys Rev Lett* **61**, 1658–1661 (1988).
83. Talantsev, E. F. & Stolze, K. Resistive transition of hydrogen-rich superconductors. *Supercond Sci Technol* **34**, 064001 (2021).
84. Talantsev, E. F. & Chistyakov, V. V. Debye temperature, electron-phonon coupling constant, and three-dome shape of crystalline strain as a function of pressure in highly compressed $\text{La}_{3-x}\text{Ni}_2\text{O}_{7-\delta}$. (2024) doi:10.48612/letters/2024-3-262-268.
85. Talantsev, E. F. & Chistyakov, V. V. A-15 type superconducting hydride La_4H_{23} : Nanograined structure with low strain, strong electron-phonon interaction, and moderate level of nonadiabaticity. *Supercond Sci Technol* **37**, 095016 (2024).
86. Talantsev, E. Quantifying the Charge Carrier Interaction in Metallic Twisted Bilayer Graphene Superlattices. *Nanomaterials* **11**, 1306 (2021).

87. Talantsev, E. F. An approach to identifying unconventional superconductivity in highly-compressed superconductors. *Supercond Sci Technol* **33**, 124001 (2020).
88. McMillan, W. L. Transition Temperature of Strong-Coupled Superconductors. *Physical Review* **167**, 331–344 (1968).
89. Dynes, R. C. McMillan's equation and the T_c of superconductors. *Solid State Commun* **10**, 615–618 (1972).
90. Chen, W. *et al.* High-Temperature Superconducting Phases in Cerium Superhydride with a T_c up to 115 K below a Pressure of 1 Megabar. *Phys Rev Lett* **127**, 117001 (2021).
91. Monni, M., Bernardini, F., Sanna, A., Profeta, G. & Massidda, S. Origin of the critical temperature discontinuity in superconducting sulfur under high pressure. *Phys Rev B* **95**, 064516 (2017).
92. Prozorov, R. & Kogan, V. G. Practically universal representation of the Helfand-Werthamer upper critical field for any transport scattering rate. *ArXiv* (2024).
93. Talantsev, E. F. Classifying hydrogen-rich superconductors. *Mater Res Express* **6**, 106002 (2019).
94. Talantsev, E. F. The Compliance of the Upper Critical Field in Magic-Angle Multilayer Graphene with the Pauli Limit. *Materials* **16**, 256 (2022).
95. Uemura, Y. J. Bose-Einstein to BCS crossover picture for high-T cuprates. *Physica C Supercond* **282–287**, 194–197 (1997).
96. Uemura, Y. J. *et al.* Universal Correlations between $\langle T_c \rangle$ and $\langle \frac{c}{n_s} \rangle$. *Phys Rev Lett* **62**, 2317–2320 (1989).
97. Talantsev, E. F. Quantifying Nonadiabaticity in Major Families of Superconductors. *Nanomaterials* **13**, 71 (2022).
98. Talantsev, E. F. Quantifying the Nonadiabaticity Strength Constant in Recently Discovered Highly Compressed Superconductors. *Symmetry (Basel)* **15**, 1632 (2023).
99. Williamson, G. K. & Hall, W. H. X-ray line broadening from fcc aluminium and wolfram. *Acta Metallurgica* **1**, 22–31 (1953).
100. Errea, I. *et al.* Quantum crystal structure in the 250-kelvin superconducting lanthanum hydride. *Nature* **578**, 66–69 (2020).
101. Steudel, R. Properties of Sulfur-Sulfur Bonds. *Angewandte Chemie International Edition in English* **14**, 655–664 (1975).